

Anomalous Platelet Transport & Fat-Tailed Distributions: A Paradigm Shift

C. Kotsalos^{*1}, K. Z. Boudjeltia², R. Dutta³, J. Latt¹, and B. Chopard¹

¹University of Geneva, Computer Science Department, Scientific and Parallel Computing Group.

²Laboratory of Experimental Medicine (ULB222), Faculty of Medicine, Université libre de Bruxelles, CHU de Charleroi.

³University of Warwick, Department of Statistics.

Abstract

The transport of platelets in blood is commonly assumed to obey an advection-diffusion equation. Here we propose a disruptive view, by showing that the random part of their velocity is governed by a fat-tailed probability distribution, usually referred to as a Lévy flight. Although for small spatio-temporal scales, it is hard to distinguish it from the generally accepted “red blood cell enhanced” Brownian motion, for larger systems this effect is dramatic as the standard approach may underestimate the flux of platelets by several orders of magnitude, compromising in particular the validity of current platelet function tests.

Keywords: platelets, anomalous transport, fat-tailed distributions, power law behavior, cellular blood flow simulations, random walks, stochastic models

1 Introduction

Platelets are entities involved in multiple physiological and pathophysiological processes such as haemostasis, thrombosis, clot retraction, vessel constriction and repair, inflammation including promotion of atherosclerosis, host defense, and even tumor growth/metastasis (1). Platelets (PLTs) are the second most numerous cell in blood, after red blood cells (RBCs), with concentration of $150\text{-}450 \times 10^9/l$. Their size, shape, material and transport properties allow them to be optimally placed as close as possible to the vessel wall, a physical requirement for the constant inspection of the integrity of the vasculature. Upon injury platelets respond rapidly (through activation, adhesion, aggregation, release reactions, etc.), and form a haemostatic plug, occluding the damaged site and preventing blood loss. Any disorder in these physiological processes results in impaired haemostasis, and inappropriate thrombus formation. For example, arterial thrombi can develop within atherosclerotic lesions resulting in stroke and heart attack, two of the major causes of morbidity and mortality in the western world (1).

In view of the involvement of platelets in the formation of thrombi, it is necessary to develop antiplatelet drugs. These drugs have been used in primary and secondary prevention for several decades now. Despite this, it appears that some patients under treatment still have a cardiovascular event. It has been therefore sought to assess the effect of these treatments and their dosage by means of platelet function tests. The results were not very conclusive. Indeed, a review article (2) has evaluated platelet functions using 6 different techniques in patients undergoing coronary stent implantation. The correlation between the clinical biological measures and the occurrence of a cardiovascular event was null for 3 of the techniques, and rather modest for the 3 others, indicating the obvious need for a more efficient tool able to monitor patient’s platelet functionalities. In another review (3), the author insists on the fact that no current test allows the analysis of the different stages of platelet activation or the prediction of the in-vivo behavior of those platelets. A more recent publication (4) reported that controlled trials have consistently failed to demonstrate a benefit of personalized antiplatelet therapy based on platelet function testing.

The role of PLTs to repair blood vessels thanks to their capability to adhere and aggregate on damaged tissues cannot be isolated from the presence of RBCs. In addition to delivering oxygen, RBCs have a significant influence on blood clotting and thrombosis (5). As a particular example of the involvement of RBCs is a rheological effect

*Corresponding author: kotsaloscv@gmail.com

known as platelet margination. In blood flow, RBCs induce a movement of platelets from the center of blood vessel to the wall. Therefore, PLTs are adjacent to the vessel wall, where they can interact to form transitory plugs in case of injury (6). Besides, this layer at the surface of the endothelium also contains plasma with coagulation factors and white cells.

Knowing how platelets travel in blood while colliding with other blood cells is still a crucial question for scientists. Indeed, how does a doctor know whether the dysfunction of platelets is only due to a modification of platelets adhesion/aggregation capabilities or due to a change of their transport properties induced by pathological RBCs? To test whether platelets dysfunction, one has to disentangle the adhesion/aggregation from their movement, as both processes are crucial for their proper functioning. Since current platelets tests, in clinical laboratory routine, do not take into account the role of RBCs in platelet transport and adhesion/aggregation processes, a better understanding and description of the RBCs-PLTs interactions seems critical to develop a new generation of platelet function tests closer to physiological reality.

In order to make a significant step in this direction, the focal point of this paper is to reveal the true mechanism of platelet transport. As we shall see, the current assumption that platelets are subject to an advection-diffusion process in the blood has to be revised.

Platelets move within blood due to the combined effect of the plasma velocity (advection) and the collisions with RBCs (enhanced diffusion). In particular, in a shear flow, PLTs experience a random motion in the direction perpendicular to the flow. The accepted description of this process (the so-called Zydney-Colton theory (7)) is that PLTs are subject to a diffusion process, whose diffusion coefficient is (8)

$$D = D_{PRP} \times (1 - H) + 0.15 \times (d_{RBC}^2 \times H/4) \times \dot{\gamma} \times (1 - H)^{1.8} \quad (1)$$

where D_{PRP} is the diffusivity of PLTs in a platelet-rich plasma (without RBCs) and its value is typically $D_{PRP} = \mathcal{O}(10^{-13}) \text{ m}^2/\text{s}$. The quantity $\dot{\gamma}$ is the shear rate, H is the hematocrit, and d_{RBC} is the diameter of a RBC.

Equation (1) gives $D = \mathcal{O}(10^{-11}) \text{ m}^2/\text{s}$, for the situation described in Chopard et al. (9), namely the diffusion of PLTs in a shear flow with $\dot{\gamma} = 100 \text{ s}^{-1}$ and $H = 0.35$, as created by the so-called impact-R PLT analyzer. This device allows one to measure the amount of PLTs that deposit on a surface perpendicular to the flow. However, based on such experimental evidence, Chopard et al. showed that if one assumes that the concentration ρ of PLTs obeys the diffusion equation

$$\partial \rho = D \nabla^2 \rho \quad (2)$$

a value of $D \approx \mathcal{O}(10^{-8}) \text{ m}^2/\text{s}$ is needed to explain the number of platelets that is observed to deposit in impact-R platelet analyzer.

This result obviously raises the question of the validity of eq. (1) or the applicability of eq. (2). The Zydney-Colton model results from accumulating experimental/theoretical data, and it has been extensively validated by numerous numerical studies, in which RBCs and PLTs were resolved (10–16). However, these studies concern spatio-temporal scales much smaller than those characterizing the impact-R device. The latter considers a layer of blood of $820 \text{ }\mu\text{m}$ of thickness, rotating in a cylinder of diameter 6.5 mm . The amount of platelets that disappear from the bulk due to their deposition on the bottom part of the cylinder is observed after 20 s . State of the art numerical simulations consider much smaller systems, usually less than $100 \text{ }\mu\text{m}$ in size, for less than 1 s of physical time.

A possibility to explain this 1000-fold difference between the Zydney-Colton theory and the effective observed diffusion is to postulate the presence of a drift term in addition to the diffusion process, as suggested in (10, 17, 18), as a general mechanism for the case of transport of deformable suspensions. This drift-diffusion model, which includes a “rheological potential” (Φ), has however an ill-considered/posed origin. Furthermore, due to the symmetry of the problem it is hard to understand why such a symmetry breaking would appear in the case of the impact-R. As a matter of fact, simulations of PLT transport in the impact-R, including an ad hoc drift term and a Zydney-Colton diffusion, do not fit so well the in-vitro time evolution of PLTs deposition (data from B. Chopard 2018).

Our claim in the present paper is that it is possible to reconcile these contradictory results by assuming that PLTs do not follow a Gaussian random walk (as is implied by the standard diffusion equation), but a random walk with a fat-tailed distribution of velocities. We show here that a very careful analysis of fully resolved blood flow simulations, in which deformable RBCs and platelets interact and move in a suspending fluid (the plasma) reveals

that collisions between RBCs and PLTs result in a power law probability distribution of PLT velocities,

$$P(v) \sim v^{-1-\alpha} \quad (3)$$

with α around 1.5 (power law exponent). We also show that for small systems, the value of the PLT mean square displacement (MSD), which is traditionally related to the diffusion coefficient, is compatible with the Zydney-Colton theory, explaining why the normal diffusion hypothesis was little questioned in the literature. But as the system size increases, we observed that the MSD increases, a behavior incompatible with a Gaussian random walk.

It should be noted that, despite this wide consensus that Zydney-Colton theory applies, a few researchers have superficially pointed out events that support our current result. Vahidkhan et al. (14, 19) observed highly anisotropic RBC distribution and a “waterfall” phenomenon (cavities that act as express lanes for platelets) affecting PLT movement (supported experimentally by Lee et al. (20)). Mehrabadi et al. (15) pointed out a possible anomalous diffusion as PLTs get trapped in the cell free layer. Yeo et al. (21) (same approach as Gross et al. (22)) who talked about anomalous diffusion of wall-bounded non-colloidal suspensions, observed exponential distributions for the densely packed spherical particles (correspondence to RBCs).

It is critical to understand, why an underlying power law behavior leads to enormous differences in transport physics. In Fig. 1, we present five particles with the same average jump length (three of them exhibit power law behavior, and two of them follow a Gaussian velocity distribution). All particles start from the same point and are left to explore the space for a thousand iterations. The particles performing Lévy flights exhibit jumps with probability density function $\sim x^{-1-\alpha}$ and an average jump of size $\alpha/(\alpha - 1)$ for $\alpha > 1$ (see Pareto distribution (23)). The ones performing Gaussian random walk exhibit jumps with a Gaussian probability density function ($\mu = 0, \sigma = 1$) and an average jump of size $\sqrt{2/\pi}$. We make sure that the average jump (\bar{J}) is the same for every particle by multiplying the individual jumps with a normalization constant equal to $\bar{J} * (\alpha - 1)/\alpha$ for the power laws, and equal to $\bar{J} * \sqrt{\pi/2}$ for the Gaussian jumps. The particles that perform Lévy flights explore the space in a completely different way than the Gaussian ones. Reconsidering platelet transport, how fast platelets reach the vessel walls is a very critical information, and inextricably associated to the underlying characteristics of the probability density function.

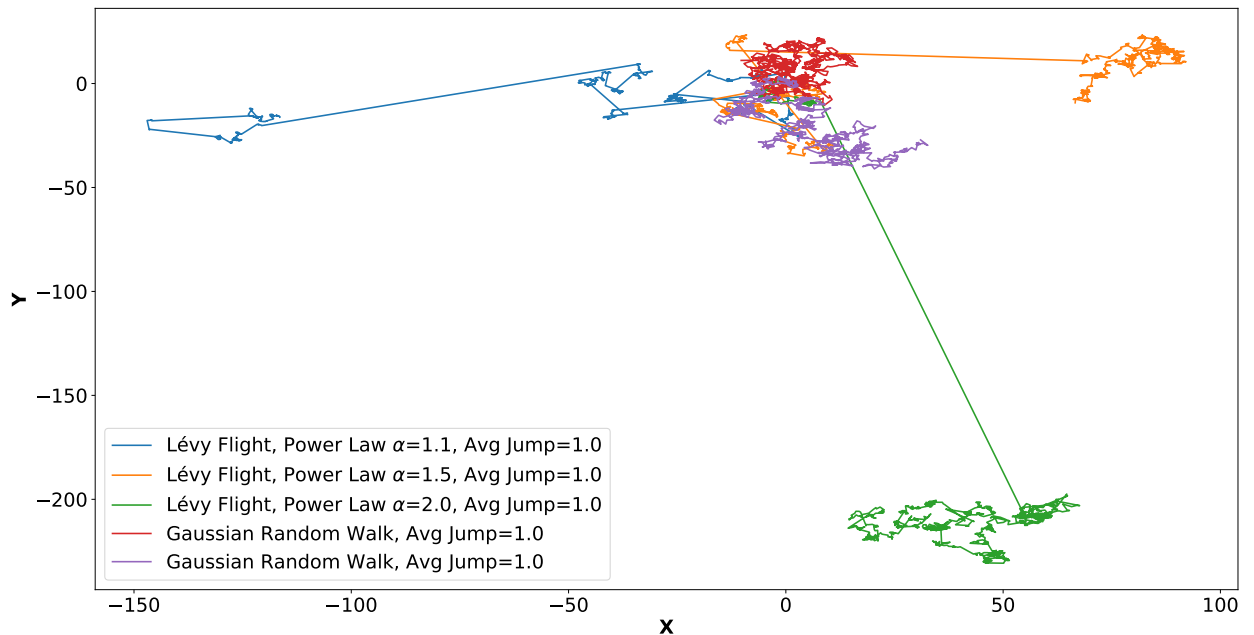


Figure 1: Random Walks with different underlying distributions. Five particles performing random walks, three of them exhibit power law behavior with varying exponent and two of them follow a Gaussian velocity distribution. The exploration of the space is largely dependent on the underlying probability density function.

This paper is organized as follows. In section 2 we describe our methodology and the numerical tools we have developed to detect the non-Gaussian behavior of PLT motion. We also explain how we can bridge the scales between the high fidelity blood flow simulations, which are extremely computationally demanding, and the PLTs displacement in the impact-R device. Our results are then presented in section 3. They consist in a careful

statistical analysis of the random motion of the simulated PLTs (coming from the fully resolved cellular blood flow simulations), and a simulation of the platelet deposition process of the impact-R (stochastic model), based on the inferred properties of the random walk. Finally, in section 4 we discuss some implications of our disrupting theory of PLT motion.

2 Methods

Our goal is to understand whether the discrepancy found in Chopard et al. (9) between the Zydney-Colton diffusion coefficient and the one accounting for the PLTs deposition pattern observed in the impact-R device can be explained by an anomalous diffusion process, thus ruling out the possibility to use eq. (2). As discussed in the previous section we made the hypothesis that PLTs may obey a fat-tailed distributed random walk instead of a Gaussian one. Due to the great difficulty to measure directly the movement of platelets (individual trajectories) in whole blood with an in-vitro approach, numerical simulations are considered. We refer to these simulations as DNS (Direct Numerical Simulations) as they provide a high fidelity description of blood, integrating RBCs and PLTs as deformable suspensions in flowing plasma. However, state of the art DNS blood solvers are still limited to rather small spatio-temporal scales. For this reason we will have to perform a very careful statistical analysis of the platelet trajectories to evidence their non Gaussian behavior at the reachable scales.

2.1 High Fidelity Blood Flow Simulations

Here we consider the Palabos-npFEM DNS blood solver (24, 25). It offers high accuracy, flexibility and high scalability on the top fastest parallel supercomputers. This computational framework couples the lattice Boltzmann solver Palabos (26) for the simulation of blood plasma (fluid phase), a finite element solver for the resolution of the deformable blood cells (solid phase), and an immersed boundary method for the coupling of the two phases. The framework resolves blood cells like RBCs and PLTs individually (both trajectories and deformed state), including their detailed non-linear viscoelastic behavior and the complex interaction between them.

Collisions between blood particles, whether RBCs or PLTs, are implemented through a repulsive force acting as a spring, when the surfaces delimiting two particles are getting too close to each other. In the current study, we employ the same parameters as reported in Kotsalos et al. (24, 25), where one can find a detailed description of the numerical models. However, the intensity of the repulsive force is varied here to account for the extra repulsion between RBCs and activated platelets whose negative charge is increased with respect to that of non-activated platelets.

We consider simulations in a 3D box as illustrated in the inset of Fig. 5. The y -axis is oriented vertically. Two horizontal no-slip walls are positioned at locations $y = 0$ and $y = L$, with $L \in \{50 \mu m, 100 \mu m, 250 \mu m, 500 \mu m\}$. A shear flow is produced in the z -direction by moving the upper wall at a proper velocity. The shear rates we consider are $\dot{\gamma} = 100 s^{-1}$ and $\dot{\gamma} = 400 s^{-1}$ (correspond to the order of magnitude for which thrombosis is observed to occur in cerebral aneurysms (9, 27)). Periodic boundary conditions are imposed along the x and z horizontal axes. This setup is meant to approximate the impact-R geometry for which $L = 820 \mu m$ and the x and z axes span a window of size $1 mm \times 1 mm$, embedded in a cylinder of diameter $6.5 mm$ (see (9) for more details). The hematocrit is $H = 35\%$ and the ratio RBCs/PLTs is around 5 (substantially larger than the physiological one, though a deliberate choice intended to provide more samples for the statistical analysis of platelet transport).

The simulations are run for a time interval $[t_0, t_1]$, which typically lasts 1 s of physical time. This interval is resolved at the scale $\sim 10^{-8} s$, the time step of the Palabos-npFEM solver. The trajectories $y_i(t)$ along the y -axis of all PLTs i are recorded, based on the position of their center of mass. From these trajectories, one has to determine the probability distribution of PLT velocities. To properly sample the time series $y_i(t)$ of positions, one has to extract the characteristic platelet mean free time, Δt , representing the average time between successive impacts/collisions. This characteristic time is important, because an under-sampling could result in missing important collision events, and thus misinterpreting the motion of platelets. On the other hand, a sampling at a too fine time scale will sample statistically dependent velocities (ballistic regime), before collisions could randomize the platelet movements (diffusive regime).

Multiple researchers define the sampling interval as $\sim \dot{\gamma}^{-1}$, but this formula has no robust explanation. Alternatively, we consider the trajectories y_i as seen at different time scale Δt , for several possible values of $\Delta t \in \{0.01 ms, 0.1 ms, 1.0 ms, 10.0 ms\}$. We compute the area A formed graphically by the trajectory $y_i(t)$ at full DNS

resolution, namely

$$A = \int_{t_0}^{t_1} y_i(t) dt \quad (4)$$

Then we compute the area formed by the trajectory at scale Δt (i.e. $y_i(t)$ with t incremented by steps Δt). These two areas should be identical if the platelet did not experience a collision during time Δt . The larger Δt for which this equality holds is chosen as the mean free time.

Fig. 2a presents this method. The vertical axis shows the relative deviation between these two areas, averaged over all PLTs and simulations. The inset shows the trajectory of one representative platelet at three different time scales. We see that $\Delta t = 1 \text{ ms}$ captures well the change in the trajectory due to collisions, while filtering out the ballistic regime. The same outcome can be retrieved from the velocity autocorrelation function (VACF) defined as

$$\text{VACF}(t) = \langle V_i(t)V_i(0) \rangle \quad (5)$$

where V_i is the DNS velocity of PLT i at the wall-bounded direction, and the average is over all platelets of the bulk. As shown in Fig. 2b, non-zero VACF (correlated velocities) mark the ballistic time scale, while zero VACF denotes the diffusive regime (random walk). Both methods (Fig. 2a & 2b) present matching results, confirming that our sampling does not result in correlated velocities.

The set of independent platelet velocities is then obtained from the quantities (where we set $t_0 = 0$ for simplicity)

$$v_i(k) = \frac{y_i((k+1)\Delta t) - y_i(k\Delta t)}{\Delta t} \quad (6)$$

for all platelets i .

A classical property characterizing the movement of platelets is their mean square displacement (MSD), defined as

$$\text{MSD}(t) = \langle (y_i(t) - y_i(0))^2 \rangle \quad (7)$$

where the average is over all platelets i of the bulk. This relation can also be written as

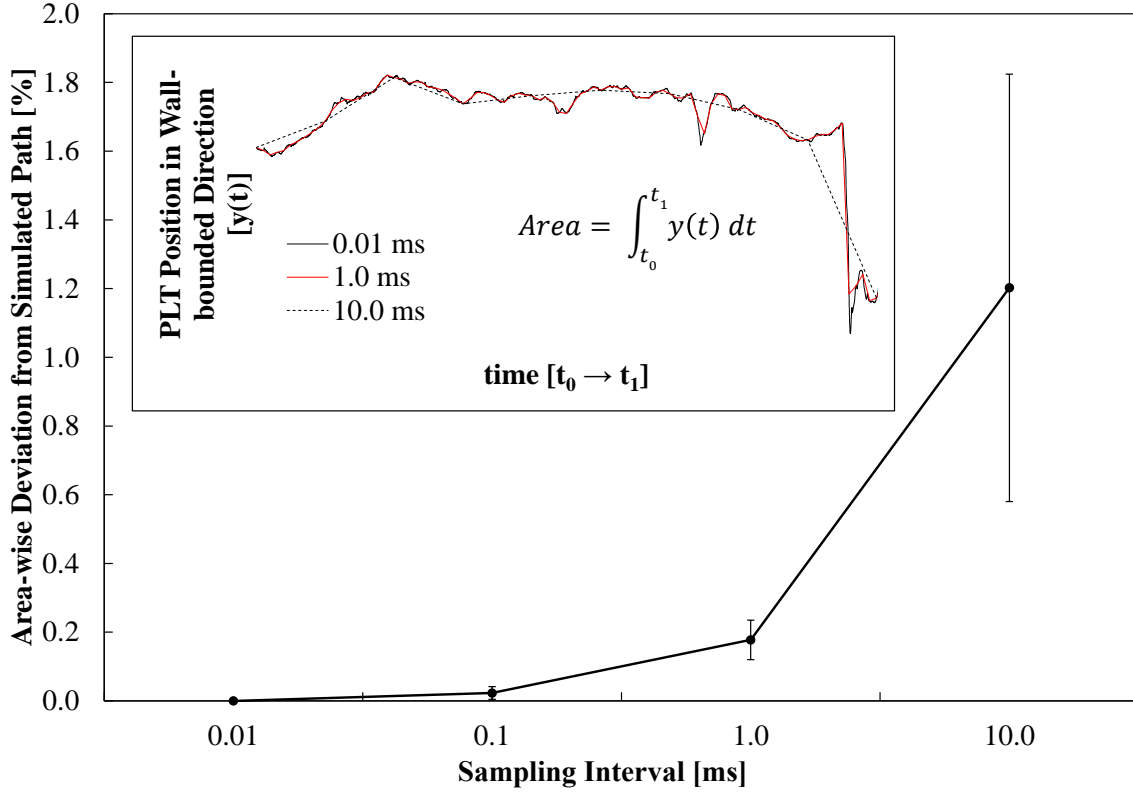
$$\text{MSD}(t) = \left\langle \sum_{k=1}^{t/\Delta t} v_i(k) \sum_{\ell=1}^{t/\Delta t} v_i(\ell) \right\rangle \quad (8)$$

Assuming that $v_i(k)$ and $v_i(\ell)$ are independent when $k \neq \ell$, and that $\langle v_i \rangle = 0$ due to the symmetry along the y axis (fact confirmed numerically for the current simulation setup), we obtain

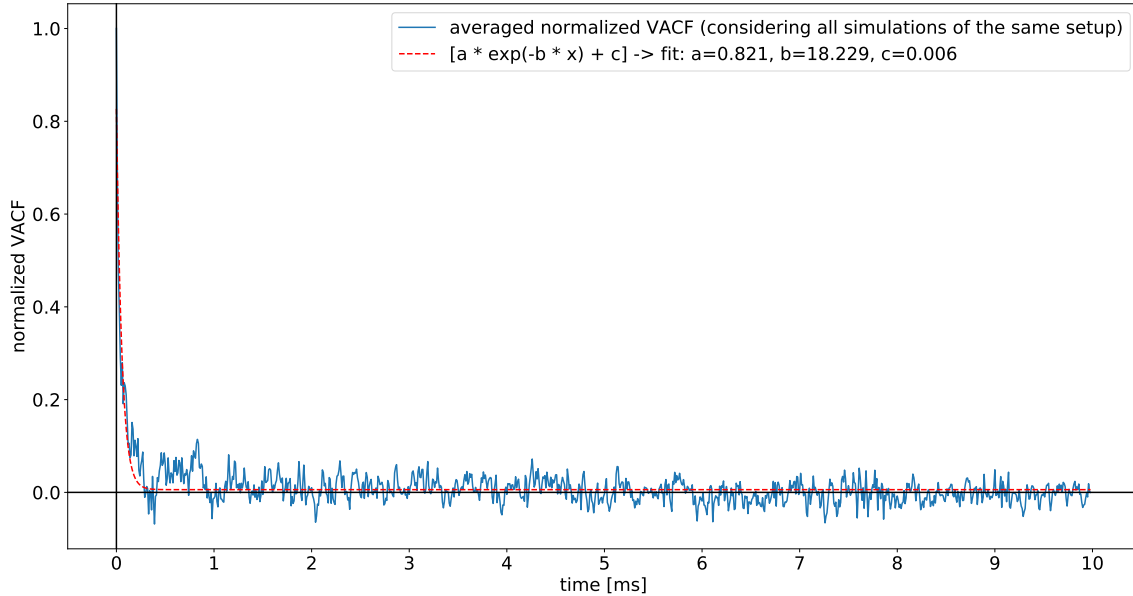
$$\text{MSD}(t) = \sum_{k=1}^{t/\Delta t} \langle v_i^2(k) \rangle = \frac{t}{\Delta t} \langle v_i^2 \rangle \quad (9)$$

The second equality comes from the fact that in a steady state, the velocity distribution is expected to be independent of time. Note however that this hypothesis is only valid in the bulk of the sample, where RBCs are found to have a constant density along the y -axis. This is no longer the case in the so-called cell-free layer, near the walls at $y = 0$ and $y = L$. For this reason, we separate the treatment of platelets according to their spatial location and determine the velocity distribution for the PLTs in the homogeneous region, away from the walls.

If PLTs encounter no other blood cell, i.e traveling ballistically, then the distance they travel would be proportional to the time interval (distance equals velocity times time), and the MSD would increase quadratically with time. In denser suspensions, quadratic behavior holds only for a very short time interval, of the order of the mean collision time. Beyond this time the motion is better described as a random walk, for which the MSD increases only linearly with time. The rate of growth of the mean square displacement depends on how often the cells suffer collisions. Equation (9) shows that $\text{MSD}(t)$ is expected to be proportional to t , but this is only the case if $\langle v_i^2 \rangle$ (variance of PLT velocities) is finite and well defined. We will show below that this is not the case for platelets in a shear flow. Actually the subtle part of this observation is that, for any numerical simulation, $\langle v_i^2 \rangle$ is obviously finite as there is a finite number of platelets in the system, for a finite number of time steps. But as the system size is increased, we observed that $\langle v_i^2 \rangle$ also increases, indicating a divergence of the variance of platelet velocities. The striking result is however that for small systems, namely those that are accessible to DNS blood flow simulations (10, 14, 15), the non-converged computed value of $\langle v_i^2 \rangle$ is compatible with the Zydney-Colton diffusion coefficient, thus supporting a misinterpretation of a Gaussian random walk.



(a)



(b)

Figure 2: Estimation of the sampling time. (a) Deviation (area-wise) from the DNS platelet trajectories as a function of the time scale at which these trajectories are observed. The way the deviation is measured is illustrated in the inset, for three different sampling intervals. The black circles in the main figure show the average deviation, computed over all platelet trajectories and simulations (DNS). The “error” bars mark the minimum and maximum deviations. One observes that a sampling interval $\Delta t = 10.0 \text{ ms}$ (dashed line in the inset) misses many collision events, but that $\Delta t = 1.0 \text{ ms}$ is a proper choice. (b) Normalized Velocity Autocorrelation Function averaged over all the simulations of the same setup (scaled impact-R device). The regime after 1 ms presents uncorrelated velocities (diffusive regime), while below this threshold there is the ballistic regime (non-zero VACF). Our sampling at $\Delta t = 1.0 \text{ ms}$ provides uncorrelated velocity samples.

2.2 Statistical Analysis of Platelet Velocities

In this section we explain how we determined the properties of the probability distribution of PLT velocities sampled from the high fidelity blood flow simulations described in section 2.1.

To avoid wall effects, we discard the velocities corresponding to PLTs that are less than one RBC diameter from the walls. In order to prove that PLT velocities are not normally distributed but have a rather high probability for extreme events, we devised a set of methods originating from analyses of fat-tailed distributions for discerning and quantifying power law behavior in empirical data (in-depth analysis by Clauset et al. (28)). A graphical explanation is provided in the Supplementary Material: Statistical Analysis.

Family of Distributions

The term “Thick Tails” is often used to describe distributions with much higher kurtosis than the Gaussian one, and “Fat Tails” is reserved for both extreme thick tails or membership in the power law class. We avoid designations such as “Heavy Tails” or “Long Tails” to keep ambiguity to a minimum (29). The term sub-exponential distributions is used for the ones that decay more slowly than an exponential, i.e. they are not exponentially bounded (popular distribution belonging to this class is the log-normal). To summarize, the degree of thick tailedness (ranking by severity) is *Thick Tailed* \supset *Sub-exponential* \supset *Power Law/Fat-Tailed (Paretian)*. Furthermore, the thick tailed and sub-exponential families have all their moments finite. We are particularly interested in the power law class to describe PLT transport, because these distributions do not have all their moments finite/defined. This happens for power law distributions whose tail decays like $\sim x^{-\alpha-1}$ with $\alpha \leq 2$ (infinite/undefined variance and moments above). For $\alpha \leq 1$ the mean of the distribution (first moment) is infinite/undefined, as well.

In statistics, we can never prove that a given distribution describes the investigated data, instead we can increase our confidence for a family of distributions against others. In our case, since we hypothesize that platelet velocities follow power law distributions with exponent $\alpha \leq 2$, we focus on finding evidences supporting this null hypothesis. Commonly used distributions that exhibit power law behavior (asymptotically) are the Pareto, Cauchy (half-Cauchy, for positive only data), Lévy, Dagum (or Burr Type III), Singh–Maddala (or Burr Type XII), Log-logistic (or Fisk), inverted Weibull (or Fréchet) (see Supplementary Material: Power Law Distributions) (23). Our approach is to check, for each DNS, the plausibility of these distributions, according to the fitting criteria presented below. Also we want to extract the asymptotic power law exponent and check how many of these distributions exhibit $\alpha \leq 2$. A question that often arises is why the Pareto alone, a pure power law, is not enough to characterize the data. Indeed, the need to consider more distributions is because Pareto fits the data fairly well toward the higher velocities, but the fit is poor toward the lower values. Thus, considering other distributions with more parameters leads to a better and unbiased fit. Afterwards, the asymptotic analysis of every distribution results in a more accurate estimation of the power exponent α (see the Supplementary Material: Power Law Distributions).

The distributions whose plausibility lowers our confidence on power laws are the normal and exponential distributions. Generally, if a power law is not a better fit than an exponential distribution, there is scarce ground for considering the distribution to be thick-tailed at all, let alone a power law (30). Regarding the sub-exponential class, a careful investigation of the sample moments can help us decide whether to disregard it or not.

Distribution Fitting

In practice, few phenomena obey power laws for all values of x (where x denotes PLT velocities). More often the power laws apply only for values greater than some minimum value, x_{min} . In such cases, we say that the tail of the distribution follows a power law (28). Thereby, for every distribution mentioned above (power law or not), we find this lower bound and perform the fitting at the tail. Regarding the remaining part of the data (body), this can be sufficiently described by the empirical distribution function (histogram - see Supplementary Material: Statistical Analysis). Note however that this procedure does not apply when fitting the data to a Gaussian. In this case, the fit is done across the whole range of velocities.

Once this lower bound x_{min} is known, every distribution is fitted on the tail using the Maximum Likelihood Estimate (MLE) method, and its plausibility is checked using the Kolmogorov-Smirnov (KS) test for goodness-of-fit. Given the symmetry of the studied phenomenon (for the current simulation setup), we use the absolute value of the velocities (no discrimination between upward and downward motions of PLTs). Thus all the statistics are one-tailed. If the p-value of the KS test is greater than the significance level (10% throughout the study for goodness-of-fit tests), then the investigated distribution could be a plausible fit to the data.

In addition to this goodness-of-fit test, we employ the Log-likelihood ratio (LLR) test (28) comparing the fitted distribution with every alternative distribution proposed above (see Family of Distributions), on the same data. In that case, the smaller the p-value of the LLR test, the more confident we can be on which distribution is a good fit of the data. The significance level for the LLR test is set to 1%. Note that, to confirm or deny a distribution, a small p-value is “good” for the LLR test (shows how trustworthy is the test’s result), while it is “bad” for the KS test (shows that the distribution is a poor fit to the data). Thus, for the acceptance/plausibility of a distribution fitted on the tail, there exist two criteria to meet, i.e. the KS and LLR tests.

The estimation of x_{min} is an optimization process based on minimizing the distance (d) between the investigated model and the empirical data (28). The metric d , that quantifies this distance, is the widely used Kolmogorov–Smirnov statistic, which is simply the maximum distance between the Cumulative Distribution Function (CDF) of the sampled DNS data (the empirical CDF, noted S), and the CDF P of the fitted model. Thus

$$d = \max_{x \geq x_{min}} |S(x) - P(x)| \quad (10)$$

Therefore, the selected x_{min} is the one that minimizes this distance. Keep in mind that for every x tested, the parameters of P are fitted using the MLE method, which requires large enough samples. Thus, the minimization process described above stops when the remaining tail has less than 100 velocities.

2.3 Bridging the scale: a Random Walk description

As indicated previously, we want to show that the unexpectedly high transport of PLTs observed by Chopard et al. (9) in the in-vitro impact-R device is compatible with the velocity probability distribution extracted from our DNS blood simulations. A direct verification is not possible as the spatio-temporal scales corresponding to the impact-R are still too hard to reach, even on the fastest supercomputers: a cubic millimeter of blood simulated for 20 seconds.

A solution to bridge this gap of scales is to disregard the detailed movement of RBCs at the level of the impact-R, and only consider the dynamics of PLTs in terms of a random walk, using the velocity distribution obtained from the statistical analysis of the fully resolved PLT trajectories in the DNS simulations. Therefore we will simulate the PLTs deposition process taking place in the impact-R through a stochastic model implementing the determined random motion of PLTs. The question is to check whether this mesoscopic transport process reproduces the number of PLTs observed to deposit at the bottom surface of the impact-R, after 20 s of operation. More precisely, the experimental data (9) show that about 3000 activated platelets per micro-liter of whole blood have disappeared from the bulk within these first 20 s.

This method follows the approach of Chopard et al. (9), by replacing the 1D diffusion equations describing the bulk of the impact-R device with actual random walks of point particles. The PLTs that cross the lower boundary are considered as deposited. Therefore, for every DNS, we perform the statistical analysis, and for every candidate of the PLTs velocity distribution, we simulate the corresponding stochastic model and record the number of deposited PLTs it predicts after 20 s. For more details on the random walks, see Supplementary Material: Statistical Analysis (Graphical Explanation) & Stochastic Model Description.

3 Results & Discussion

Our analysis builds upon the research by Chopard et al. (9). In more details, in the in-vitro part of their study the researchers used the impact-R platelet function analyzer to study the evolution of PLT deposition (adhesion-aggregation processes) on the substrate of the device. Impact-R is a cylindrical apparatus (L=820 μm height), whose lower end is a fixed disc (deposition surface, 132.7 mm^2), and its upper wall is a rotating disc. Due to the rotating upper wall, the blood is subject to a pure shear flow. The imposed constant shear rate was 100 s^{-1} (inside an observation window of $1 \times 1 mm^2$), and the blood was extracted from seven healthy donors. The differential role of activated and non-activated platelets was analyzed, as well as the role of albumin in the deposition process. The in-silico counterpart of their study consisted of 1D diffusion equations describing the movement of activated platelets (AP) and non-activated platelets (NAP) in the bulk of the device, and of stochastic rules for PLT deposition on the substrate. The study revealed that the Zydney-Colton (7) shear induced diffusion coefficient (D) was significantly too small to explain the observed deposition rate.

The fully resolved 3D cellular blood flow simulations (DNS, section 2.1) provide a great amount of information, that simplified mechanistic models or in-vivo/vitro experiments cannot provide. Numerically following individual

particles and resolving the complex interactions, helped us develop an alternative theory on how platelets are transported. We tried to reproduce numerically the in-vitro experiments performed in Chopard et al. (9), to the extent possible, given the high computational cost. To reduce the computational demand, we designed our numerical simulations in channels with lateral dimensions of $50 \mu m$, while resolving the wall-bounded direction at $L=\{50, 100, 250, 500\} \mu m$. Consider that the in-vitro counterpart consists of $1000 \mu m$ in the lateral directions, and $820 \mu m$ in the wall-bounded direction. Numerically, we generated a constant shear rate flow regime at $100 s^{-1}$, realized with the help of a moving top wall and a fixed bottom wall. Periodic boundaries were applied in the flow and vorticity directions, and the hematocrit was 35%, as in the experiments.

Regarding the platelet size and shape, we considered numerical experiments with either activated or non-activated PLTs. The NAP are simulated as nearly-rigid oblate ellipsoids with diameters $\{2.5, 3.6\} \mu m$, thicknesses $\{0.6, 1.1\} \mu m$, and volumes $\{2.0, 7.0\} fl$, respectively. The AP are simulated as nearly-rigid spheres with diameters $\{3.0, 3.6, 4.0, 5.0\} \mu m$ (covering the uncertainty from the complicated shape transformations), and volumes $\{12, 22, 30, 60\} fl$, respectively. Upon PLT activation, negatively charged phospholipids are translocated from the inner membrane to the external surface, leading to a more negatively charged PLT. This complex electrochemical behavior is quantified by the electrophoretic mobility of platelets (31–33). Additionally to the change of the electrophoretic mobility, there is a severe change in shape with the appearance of blebs and pseudopods, which increases the hydrodynamic volume of AP. While we address the latter alteration through the spherical shape, the complex electrochemical behavior is roughly resolved through an increase in the intensity of the collision potential between activated PLTs and RBCs, i.e. increased repulsive forces ranging from 5 to 10 times compared to the ones of NAP.

As for the RBCs, the normal biconcave shape is used in the majority of the experiments, while in few of them we introduced spherised RBCs emulating pathological conditions (27), e.g. diabetes, chronic obstructive pulmonary disease.

We performed 64 simulations on Piz Daint, the flagship system of the Swiss National Supercomputing Center, which is one of the fastest supercomputers in the world. These simulations include for completeness, 5 case studies in a tube of $50 \mu m$ diameter, 5 case studies at 20% hematocrit, and 6 case studies with constant shear rate at $400 s^{-1}$. Forty-one simulations follow the “exact” same setup as the experiments of Chopard et al. (9), but all 64 present qualitatively the same platelet transport behavior. Out of the 41 simulations, 22 deal with AP (12 of them include repulsive forces), and the rest deal with NAP. The graphs and results presented below include these 41 simulations.

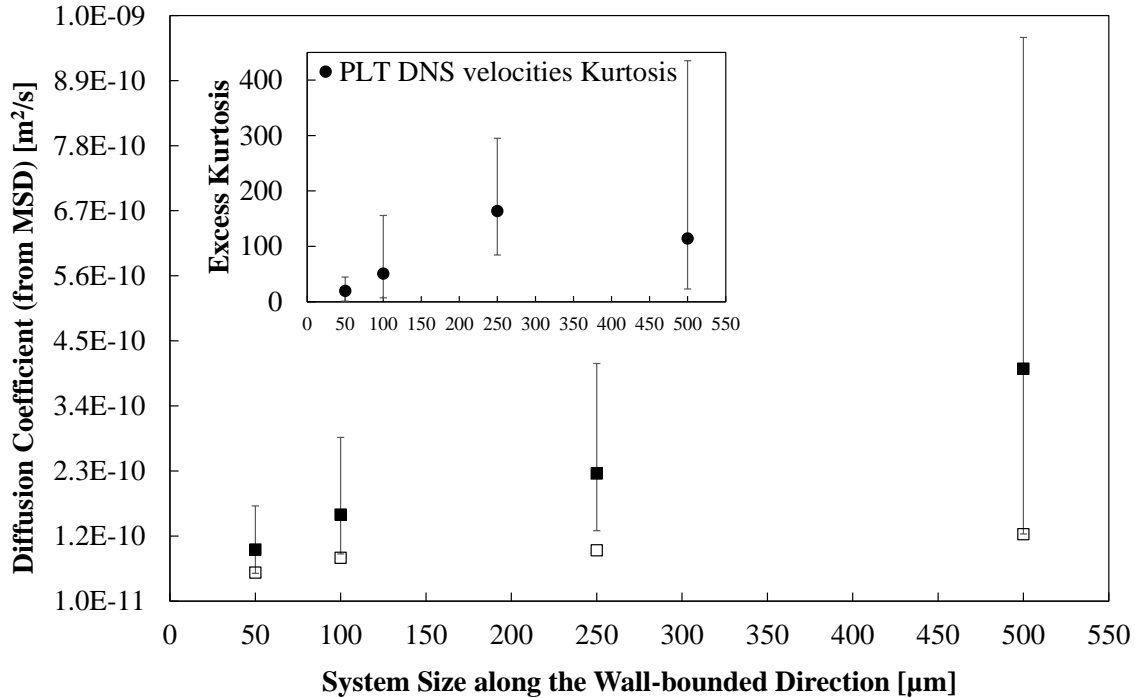
3.1 Anomalous Transport Manifested in Geometry

A standard diffusive process is unaffected by the size of the system (at least away from the walls), i.e. the moments (e.g. variance, kurtosis) of PLT velocities should converge as the sample size increases. Fig. 3 presents the diffusion coefficient D of PLTs (AP/NAP) when extracted from the mean squared displacement (sampled DNS), for channels of varying sizes. Traditionally, the diffusion coefficient is linked to the MSD, as $D_{MSD} = MSD(t)/(2t)$ for 1D systems, e.g. along the wall-bounded direction. The black square points in Fig. 3 indicate the value of D_{MSD} as a function of the system size, averaged over all DNS simulations. The “error” bars denote the minimum/maximum coefficients among the various DNS.

In Fig. 3 we also evaluate the PLT diffusivity D_{Gauss} (empty squares), when a Gaussian distribution is (poorly) fitted on the observed PLT velocities. The D_{Gauss} is computed from the standard deviation of the corresponding normal distribution. As expected, the latter approach returns a diffusion coefficient that is not affected by the system size (small variations are due to different parameters in the DNS). However, for the diffusivity emerging from the MSD, there is a diverging behavior as the sample sizes increase, a signature of a fat-tailed velocity distribution (diverging second central moment/variance with which MSD is linked to, section 2.1). On top of this observation, we show in the inset of Fig. 3 the mean excess kurtosis (fourth standardized moment) of platelet velocities, which presents a diverging behavior as well, and values that are way higher than the corresponding null value of a normal distribution.

Alongside with observing the moments of the sampled data, we performed a number of normality tests to check if a Gaussian distribution is a plausible model for the data. We deployed the Shapiro-Wilk, D’Agostino’s K^2 and Anderson-Darling normality tests to check this hypothesis. As expected, every normality test consistently rejected this hypothesis.

Summarizing, the extremely high kurtosis ($\gg 0$), the failed normality tests, and the diverging moments of PLT velocities are the first signs of fat-tailed distributions, and more specifically they indicate presence of power laws



■ PLT Diffusion Coefficient (MSD DNS) □ PLT Diffusion Coefficient (Gaussian Random Walk)

Figure 3: Diverging moments indicate fat-tailed distributions. PLT diffusion coefficient D (black squares) estimated from the mean square displacement of PLTs, computed from the DNS. The values of D are given as a function of the size L along the y axis obtained by an average over all the simulations. The “error” bars denote the minimum/maximum coefficients among the various DNS. The white square indicates the diffusion coefficient that would correspond to a Gaussian random walk by forcing a normal distribution fit on the measured PLT velocities. The inset presents the mean excess kurtosis of PLT velocities coming from the DNS, as a function of L . The “error” bars correspond to the min/max values of the kurtosis. The diverging moments clearly indicate fat-tailed distributions with infinite/undefined moments (power law behavior with exponent $\alpha \leq 2$).

with exponents less than 2, i.e. infinite/undefined variance (second central moment) and moments above. A striking observation is that the resulting diffusion coefficients from our numerical experiments are not far from the Zydney-Colton model (7) or other numerical studies (10, 14, 15), i.e. they are consistently two to three orders of magnitude higher than the Brownian diffusivity $\mathcal{O}(10^{-13})$ m^2/s . As well accepted, our simulations confirm the role of PLTs-RBCs collisions to enhance PLTs transport, but a further analysis implies that the diffusive process is anomalous. Possibly, the suggestion for extra drift terms or rheological potentials (10, 17, 18) comes from a misinterpretation of this anomalous diffusive process.

3.2 Power Law Emergence

From the statistical analysis of the sampled DNS output, we tried to find evidences that PLT velocities follow fat-tailed distributions, and more specifically power laws with exponent $\alpha \leq 2$. Out of the 41 numerical experiments only 2 of them did not show evidence of our hypothesis, i.e. no valid fitting of power laws on the data was obtained. For the rest, the tails of PLT velocities can be described with distributions which asymptotically behave as power laws (see Family of Distributions in section 2, and the Supplementary Material: Power Law Distributions). Fig. 4 gathers the PLT velocities from the 41 numerical simulations. The histogram uses logarithmically spaced bins to accurately capture the tail of the distribution. The velocities are discriminated as upward/downward validating the symmetry of the setup, i.e. a PLT has equal chance to move up or down. Given this observation, the statistical analysis is performed on the absolute value of the velocities. Additionally, Fig. 4 shows an exponential fitting on the data, which clearly fails to capture the decay of the tail. Indeed, the tail regime (white background of Fig. 4) presents a power law behavior, i.e. straight line in a log-log plot of the histogram. The Pareto curve plotted in Fig. 4 is just for visualization purposes, since the statistical analysis should be performed per DNS. As mentioned by Clauset et al. (28), the regression methods on doubly logarithmic histograms give significantly biased exponents,

and thus our statistical analysis deploys robust tools, other than plotting & fitting, to reveal the unbiased power law exponent α .

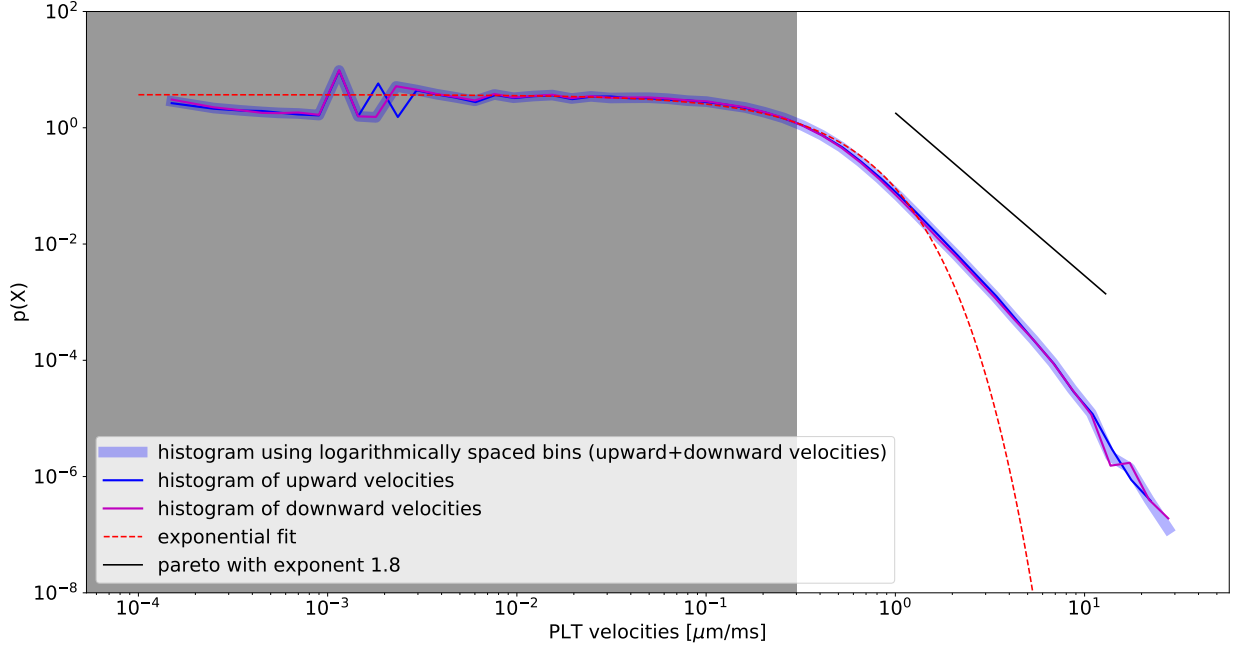


Figure 4: Histogram of PLT velocities on doubly logarithmic axes using logarithmically spaced bins. The shaded area is the body of the distribution, which is of no interest for the current analysis, while the non-shaded area roughly presents the tail of the data. The histogram accumulates the velocities from all the numerical experiments performed, discriminating their upward or downward direction, and thus revealing the symmetry of PLT motion in the current setup (impact-R device). An exponential distribution fails to describe the decay of the tail, while it is evident that a power law fits better on the data.

Table 1 shows, for the different platelet types (non-activated platelets NAP, activated platelets AP-no rep, activated platelets with repulsive forces AP-rep), the power law exponent α averaged over all the DNS experiments and the fitted/accepted power laws with exponent ≤ 2 . The min/max indicated in table 1 denote the minimum and maximum values of the exponent from the fitting of the various distributions (Pareto, half-Cauchy, Lévy, Dagum, Singh–Maddala, Log-logistic, and inverted Weibull) for each PLT type. A remark is that we are not biased towards the exponents ≤ 2 (discarding the values above), since our previous observations, i.e. on diverging moments, high kurtosis and failed normality tests, support this direction, and in parallel reject the alternative hypothesis on thin-tailed distributions.

It is interesting to observe that the shape and the electrophoretic properties of platelets are reflected on the exponent of the power law. The lower the power law exponent, the higher the mobility through “extreme” tail events. The exponents observed for AP-rep are consistently smaller. In the Supplementary Material: Summary of DNS and Statistical Analysis, we provide a table that summarizes the majority of the performed experiments with key quantities per DNS for the completeness of the study, e.g. one can find per DNS the power law exponents (considering all fitted/accepted distributions with exponent $\alpha \leq 2$).

In a second step, we used the fitted distributions as generative mechanisms for simulating random walks and the transport of PLTs in the impact-R device. Table 1 presents the amount of deposited PLTs (the ones that cross the bottom wall) after running the stochastic simulations for 20 s of physical time, with $L = 820 \mu m$. Chopard et al. (9) report that 3125 AP have disappeared from the bulk during these 20 s, with an initial concentration of 4808 AP per micro-liter. Given that the phenomenon is symmetric along the y -axis (cross-checked with the DNS), and due to the developed cell free layer close to the walls (trapping the crossing PLTs), we expect at least 1500 platelets out of 4808 ($1500 \sim 3125/2$) to cross the bottom wall of the system.

Table 1 shows that this expected number of deposited platelets is compatible with the proposed fat-tailed velocity distribution, without the need to invoke special drift terms or a rheological potential. The table also presents the amount of deposited PLTs when forcing a Gaussian or exponential fit on the velocity distributions. Clearly, the

Table 1: Power law exponent and deposition rates. Mean power law exponent for the different PLT types, averaged over the simulations and power law distributions (the ones that give $\alpha \leq 2$). The min/max denote the variation of the exponent across the simulations. The simulated (random walk model) mean number of deposited PLTs in the impact-R is computed considering all the simulations and power law distributions (the ones that give $\alpha \leq 2$) per PLT type. The maximum deposition corresponds to the lowest power law exponent (fatter tails). The mean deposited PLTs based on a (poor) fitting of normal or exponential distributions heavily underestimate the deposition observed in Chopard et al. (9).

	NAP	AP - no rep	AP - rep
Mean Power Law α (min/max)	1.56 (1.35/1.75)	1.48 (1.23/1.75)	1.40 (1.12/1.65)
Mean Deposited PLTs (power laws)	366	321	416
Max Deposited PLTs (power laws)	1759	1512	2270
Mean Deposited PLTs Normal Distribution	246	174	287
Mean Deposited PLTs Exponential Distribution	250	175	290

deposition values are way too small to describe the deposition rates observed in the in-vitro experiments. Therefore, the use of standard diffusive models heavily underestimates the deposition rate, compared to the Lévy flights that produce a 2 to 10 times higher amount of deposited PLTs.

As shown in Fig. 5, it is also interesting to note that as opposed to the MSD which diverges with the system size, the exponent α keeps a consistent value when varying L from 50 μm to 500 μm (scale-invariance of power laws, i.e. the phenomena are expected to occur without a characteristic size or scale).

4 Conclusions

Combining the power law fitting on the tails with the normality tests that fail in all the experiments, the diverging moments of the velocity distribution, the very high kurtosis, and the good agreement with the impact-R deposition data, we give convergent evidences that PLTs do not follow a Gaussian random walk, but rather Lévy Flights. Therefore, it is the properties of the system that lead us towards the validation of our hypothesis. The standard diffusion equation does not apply to describe PLTs transport. Fractional differential equations might be needed to account for such an anomalous diffusion process at the macroscopic scale.

As mentioned by Kumar and Graham (18), no clear and systematic mechanistic explanation was yet proposed for the segregation and margination phenomena of platelets. In particular, no simplified mathematical description (such as a set of transport equations or a simple stochastic process model) has emerged that captures the phenomena. In this study, we prove that PLT velocities, more specifically the tail of their distribution, can be described by power laws ($P(v) \sim v^{-\alpha-1}$) with exponent $\alpha \leq 2$. We found no evidence of normally distributed PLT velocities, and thus PLTs cannot possibly exhibit standard diffusion, which is the norm when describing PLT transport.

The new stochastic process model that we introduce does not need additional terms to describe margination, as is the case in other studies (10, 15, 17). A striking observation is that while our results are compatible with the standard models (diffusion coefficient extracted from MSD), a further investigation (statistical analysis) reveals the anomalous behavior of PLT transport. This can be explained from the fact that the more fat-tailed a distribution, the more statistical information lies in the tail, and the moments (on which standard diffusive models are built upon) become uninformative and unreliable. The majority of the numerical research in this field is limited to case studies that deal with too few blood cells in the computational domain, and this is due to the high computational cost of the simulations. Our highly scalable numerical framework allows us to investigate cases with dimensions approaching the ones of the in-vitro experiment. We would like to emphasize that the ability to study sizes of clinical relevance (at least resolving the direction of interest), allowed us to observe the idiosyncratic behavior of PLT transport, and to capture the anomalous characteristics that manifest in setups of larger sizes.

For the current study, based on in-vitro experiments (9), we limited the exploration of the parametric space to 35% hematocrit and low shear rates. Given that platelet transport is a collision-driven phenomenon, we believe that there should be a limit between 0 (PLT rich plasma) and 35% hematocrit, below which the normal diffusion is restored. We have performed a handful of numerical experiments at 20% hematocrit revealing that anomalous transport is still occurring provided that repulsive forces (activated PLTs) are present. On the other hand, there was no evidence for anomalous transport of non-activated PLTs at this low hematocrit value. More in-vitro &

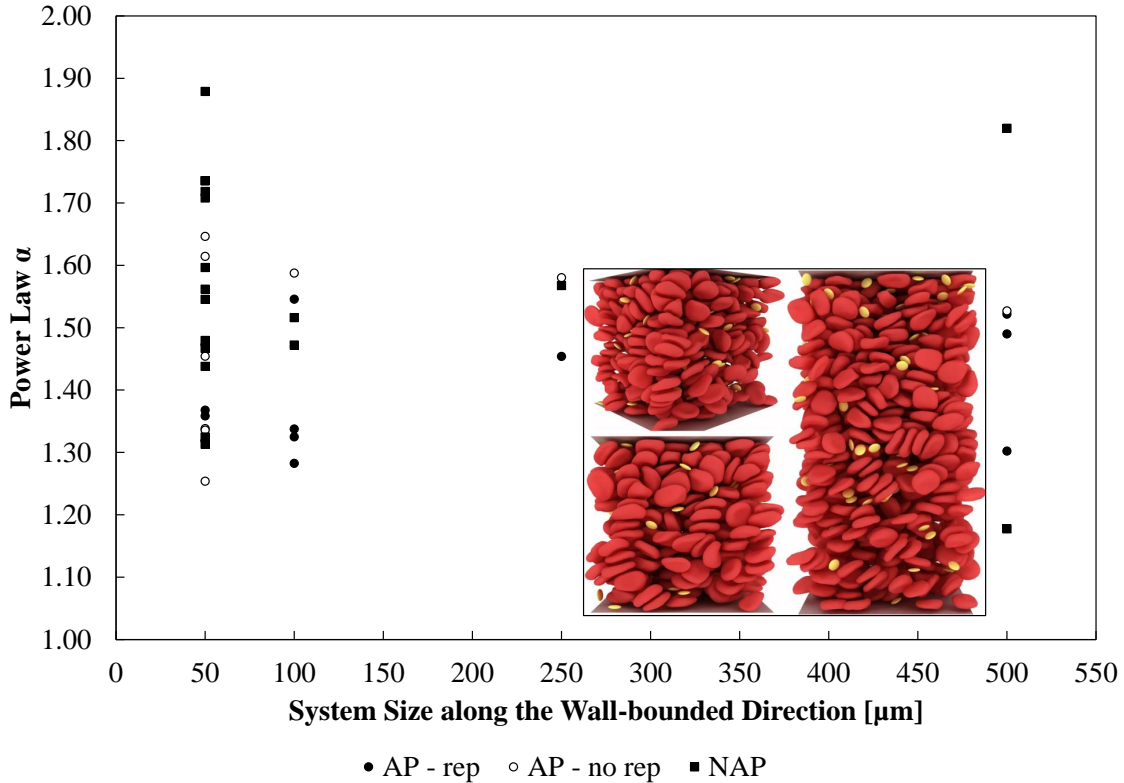


Figure 5: Power law exponent invariance. Mean power law exponent per cellular blood flow simulation. The power laws are independent of the system size (no diverging behavior as with the moments of the velocity distribution). Any variation is due to the different parameters per simulation (shapes, sizes, repulsive forces). The inset shows a few simulation snapshots from systems of size 50 & 100 μm along the wall-bounded direction y .

in-silico experiments are critical to shed light on this new interpretation of PLT transport, and to determine the power law exponent as a function of the shear rate and hematocrit.

In addition to proposing a disruptive view of PLT transport physics in blood, our results have a concrete impact on the design of new and efficient platelet function tests. Those can be a vital part for the detection of cardio/cerebrovascular diseases in clinical practice. Nowadays, there exist numerous platelet function tests for the diagnosis of disorders or the monitoring of anti-platelet therapies, but with limited prognostic capacity in clinical practice due to contradicting results. As several studies show (2–4), there is a problem interpreting the results and mapping them to patient risk and disease. We strongly believe that the emerging stochastic models from the present analysis will offer a paradigm shift for developing the next generation tests, as the understanding of PLT transport is inextricably associated with the success of platelet function testing. A first step in this direction was proposed by Dutta et al. (34), a study in which clinically important properties, such as platelet adhesion and aggregation rates, can only be properly inferred provided that PLT transport can be correctly described.

Supplementary Material: Statistical Analysis (Graphical Explanation)

For every cellular blood flow simulation, we produce from the sampled output the histogram of the absolute platelet velocities (velocities along the wall-bounded direction for channel flow, and radial velocities for tubular flow). Our goal is to fit a model on this histogram and use it for simulating random walks. Below some lower bound (x_{min}), the original data can be sufficiently described by the empirical distribution function (histogram), but above x_{min} , due to the fractionate information that we get from the tail, we need to apply more sophisticated statistical models. Since we are particularly interested on investigating the power law hypothesis, we fit a family of distributions that asymptotically exhibits power law behavior (23), e.g. Pareto, half-Cauchy, Lévy, Dagum, Singh–Maddala, Log-logistic, and inverted Weibull. Every distribution is fitted separately on the data (just at the tail), and therefore the lower bound and power law exponent α vary per distribution (see figure 6). The distributions with $\alpha \leq 2$ are characterized as fat-tailed or power laws, and their exponents (presented as mean, minimum & maximum per DNS) describe the fatness of the tail, i.e. the lower the exponents the higher the tail events (large PLT velocities). This analysis is performed for every cellular blood flow simulation, and the resulting power law exponents are grouped/presented per PLT type (activated, non activated, and with/without repulsive forces).

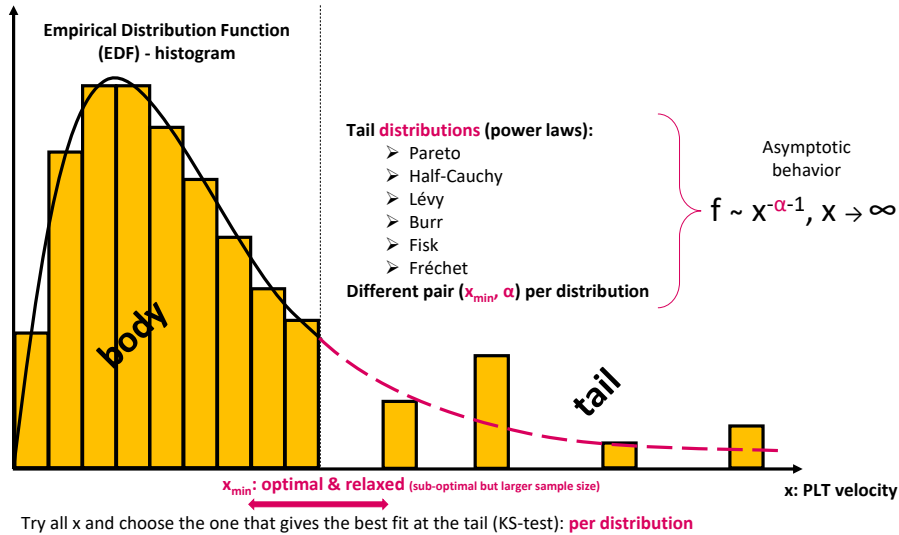


Figure 6: Statistical analysis per direct numerical simulation. Per investigated distribution, we define x_{min} with the optimization process as described in Methods, and α through the MLE method.

To generate data for the random walks, the DNS sampled output (per simulation) is split into the body and the tail (see figure 6). Regarding the body, we use the empirical distribution function (ECDF) for generating new velocities. For the generated velocities that are above the x_{min} (varies per fitted distribution), we use the fitted distributions to re-generate velocities belonging to the tail. For the new data to be as close as possible to the original (from DNS), the fitted distributions should pass the goodness-of-fit and LLR tests. Assuming a plausible distribution for the tail, it may be the case that the tail sample size is small ($n \approx 100$). Fitting on samples of small sizes should be treated with caution, because power laws may appear to be a good fit even when the data are drawn from a non-power law distribution. An additional step to strengthen our confidence on power law behavior is to relax the x_{min} threshold, i.e. reduce the lower bound and thus increase the sample size on which to fit. For this relaxed version, we need to perform an additional goodness-of-fit test (28). For this test, we use as metric the Kuiper’s statistic, which is a variation of the Kolmogorov-Smirnov, but more sensitive on capturing differences at the tails. In short, we generate data from the ECDF, then synthetic data with the optimal x_{min} (below x_{min} we use the ECDF, above x_{min} we use the fitted model), and we compare the two data sets using the Kuiper’s test, from which we get the statistic. Following, we generate another set of synthetic data with the relaxed x_{min} , and we compare it with the data from the ECDF, extracting another statistic. If the last statistic is smaller than the one of the first comparison, then the relaxed model is a valid alternative. By repeating this process more than a thousand times (28), we get a p-value coming from the fraction of valid/accepted relaxed models to the overall repetitions. Keep in mind, that the relaxed tail gives an additional fitting for consideration, thus for each distribution we have the *optimal and relaxed fittings*. Therefore, per DNS and per fitted distribution, we construct a generative mechanism that “feeds” the random walk models.

Supplementary Material: Power Law Distributions

The probability densities presented here are in the “standardised” form, i.e. the location parameter is zero and the scale parameter is one. However, the analysis is not affected by this “standardised” form, since these parameters are only for shifting and scaling the investigated distributions, respectively. The power law exponent α is given by the asymptotic analysis of the distributions (probability density function-pdf), which decay like $f \sim x^{-\alpha-1}$. The presentation of the pdf with -1 in the exponent is deliberate, since the survival function ($\bar{F} = Pr(X > x)$, complementary cumulative distribution function) decays like $\bar{F} \sim x^{-\alpha}$.

Pareto

The probability density function for Pareto is: $f(x, b) = \frac{b}{x^{b+1}}$ for $x \geq 1$, $b > 0$. For $x \rightarrow \infty$, $f(x, b) \sim x^{-b-1}$. The variance is ∞ for $b \leq 2$ and the mean is ∞ for $b \leq 1$. The power law exponent is b .

Half-Cauchy

The probability density function for half-Cauchy is: $f(x) = \frac{2}{\pi(1+x^2)}$ for $x \geq 0$. For $x \rightarrow \infty$, $f(x) \sim x^{-2}$. The mean and variance are undefined. The power law exponent is fixed to 1.

Lévy

The probability density function for Lévy is: $f(x) = \frac{1}{\sqrt{2\pi x^3}} \exp\left(-\frac{1}{2x}\right)$ for $x \geq 0$. For $x \rightarrow \infty$, $f(x) \sim x^{-1.5}$. Both the mean and the variance are ∞ . The power law exponent is fixed to 0.5.

Dagum (or Burr Type III)

The probability density function for Dagum is: $f(x, c, d) = cdx^{-c-1}/(1+x^{-c})^{d+1}$ for $x \geq 0$ and $c, d > 0$. For $x \rightarrow \infty$, $f(x, c, d) \sim x^{-c-1}$. The mean is undefined for $c \leq 1$, and the variance is undefined for $c \leq 2$. The power law exponent is c .

Singh–Maddala (or Burr Type XII)

The probability density function for Singh–Maddala is: $f(x, c, d) = cdx^{c-1}/(1+x^c)^{d+1}$ for $x \geq 0$ and $c, d > 0$. For $x \rightarrow \infty$, $f(x, c, d) \sim x^{c-1}/x^{cd+c} \sim x^{-cd-1}$. The mean is undefined for $cd \leq 1$, and the variance is undefined for $cd \leq 2$. The power law exponent is cd .

Log-logistic (or Fisk)

The probability density function for Log-logistic is: $f(x, c) = cx^{-c-1}(1+x^{-c})^{-2}$ for $x \geq 0$, $c > 0$. For $x \rightarrow \infty$, $f(x, c) \sim x^{-c-1}$. The mean is undefined for $c \leq 1$, and the variance is undefined for $c \leq 2$. The power law exponent is c .

Inverted Weibull (or Fréchet)

The probability density function for inverted Weibull is: $f(x, c) = cx^{-c-1} \exp(-x^{-c})$ for $x > 0$, $c > 0$. For $x \rightarrow \infty$, $f(x, c) \sim x^{-c-1}$. The mean is undefined for $c \leq 1$, and the variance is undefined for $c \leq 2$. The power law exponent is c .

Supplementary Material: Stochastic Model Description

The Impact-R is a cylindrical device whose bottom wall is a fixed disc (deposition substrate), while the upper wall is a rotating disc (shaped as a cone with a small angle). The height of the device is 0.82 mm and due to the motion of the upper wall a pure shear flow is created. A controlled shear rate $\dot{\gamma}$ is produced in a given observation window of $1 \times 1 \text{ mm}^2$, where we track the formation of clusters resulting from the deposition and aggregation of platelets.

The platelets reach the bottom layer due to a RBC-enhanced shear-induced diffusion. This process is described by a random walk as

$$\begin{aligned}\Delta z(t) &= \lambda v_z |s_z| dt \\ \Delta x(t) &= v_{xy} |s_{xy}| \cos(2\pi r) dt \\ \Delta y(t) &= v_{xy} |s_{xy}| \sin(2\pi r) dt\end{aligned}$$

where $v_{z,xy}$ are speed units coming from the DNS, r is a random variable uniformly distributed in $[0, 1[$, $s_{z,xy} \in]0, \infty[$ are random variables distributed according to the fitted models from the cellular blood flow simulations, $\lambda \in \{-1, 1\}$ with probability $1/2$ for each outcome (given the proven symmetry of the current setup), and dt is the time step of the simulation. The random motion in the xy -plane can be omitted for simplicity. Superimposing the stochastic motion with the velocity field of the pure shear flow, the positions of the platelets are updated as

$$\begin{aligned}z_i(t + dt) &= z_i(t) + \Delta z_i(t) \\ x_i(t + dt) &= x_i(t) + \Delta x_i(t) + \dot{\gamma} z_i dt \\ y_i(t + dt) &= y_i(t) + \Delta y_i(t)\end{aligned}$$

The AP and NAP crossing the lower boundary of the computational domain are candidates for deposition (trapped in the Cell Free Layer -CFL-, and never re-injected into the bulk), periodic conditions are applied at the x, y directions, and bounce back boundary condition for the platelets that cross the upper boundary. To simplify our analysis and get a rough estimate of the deposited PLTs, we do not consider any deposition rule (as in Chopard et al. (9)), but we assume that a PLT deposits when it crosses the lower boundary. Figure 7 summarizes this stochastic process.

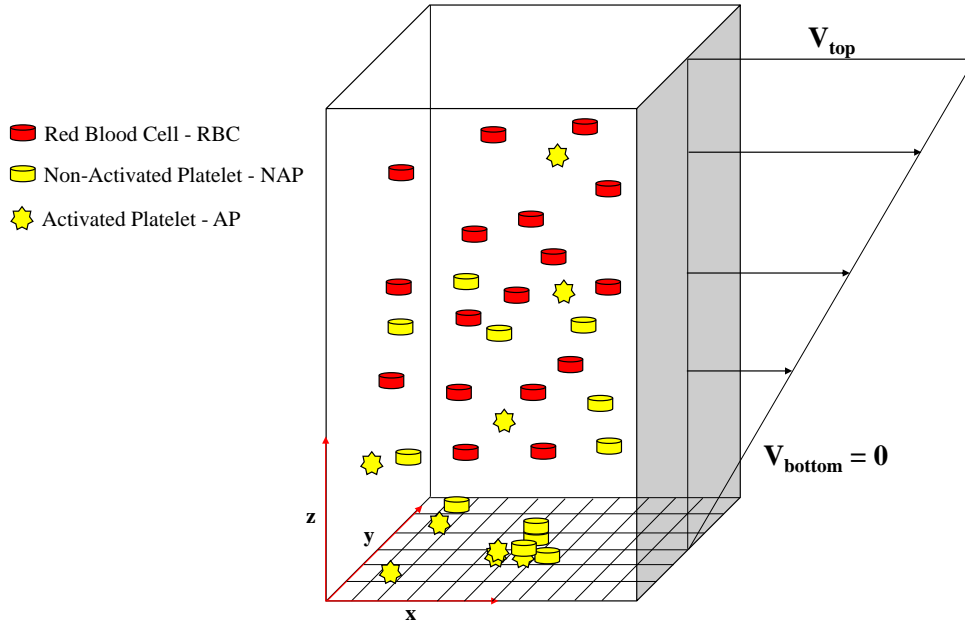


Figure 7: Window of Impact-R device: The bottom wall is a fixed boundary of dimensions $1 \times 1 \text{ mm}^2$, the wall-bounded direction is 0.82 mm . The bulk contains whole blood at 35% hematocrit. The discretization of the substrate is such that in every cell can fit just one platelet. The initial densities of the blood particles are determined by the *in vitro* experiment (9) and usually are about: $172\,200 \text{ } (\mu\text{l})^{-1}$ for NAP, $4808 \text{ } (\mu\text{l})^{-1}$ for AP.

Supplementary Material: Summary of DNS and Statistical Analysis

PLT: Activated/Non-Activated platelets, *rep*: no repulsive forces at 20 (weight of collision potential-DNS related), *exp*: either scaled impact-R (box) or tube, *dir*: system size along the wall-bounded direction/diameter [μm], *Ht*: hematocrit [%], *SR*: Shear Rate [s^{-1}], *num RBCs/PLTs*: number of RBCs/PLTs in DNS, *vel*: mean absolute velocity along *dir* from DNS [$\mu\text{m}/\text{ms}$], *D (DNS)*: Diffusion Coefficient - MSD of DNS [m^2/s], *D (Gaussian)*: Diffusion Coefficient - Random Walk (Gaussian fitted on DNS) [m^2/s], *fat-tails*: number of accepted power laws (considering only the ones with $\alpha \leq 2$) for both optimal and relaxed tail fitting, *min sample size*: minimum sample size of one of the accepted power laws, *avg sample size*: average sample size considering all accepted power laws, *avg exp*: average power law exponent considering all accepted power laws, *max depo*: deposited PLTs (after 20s physical time (9)) using the random walks (Impact-R at full scale) corresponding to the *min exp*. Simulations that seem to repeat are with/without the Particle In Kernel (PIK) technique (25) (validating its consistency).

PLT	rep	exp	dir	Ht	SR	num RBCs	num PLTs	vel	D (DNS)	D (Gaussian)	excess kurtosis	fat-tails	min sample size	avg sample size	avg exp	min exp	max exp	max depo
AP	200	box	500	35	100	4765	953	0.329	3.00E-10	1.12E-10	23.3	2	640	822	1.522	1.35	1.70	367
AP	200	box	500	35	100	4765	953	0.319	3.11E-10	1.01E-10	31.4	3	362	619	1.302	1.00	1.63	384
AP	200	box	50	35	100	476	95	0.367	1.40E-10	1.27E-10	17.5	4	181	772	1.319	1.00	1.59	640
AP	200	box	50	20	100	272	54	0.218	1.54E-10	4.87E-11	5.4	3	104	540	1.314	1.00	1.49	413
AP	200	box	100	35	100	953	190	0.419	2.87E-10	1.77E-10	26.8	2	508	3081	1.325	1.30	1.35	879
AP	200	box	50	35	100	476	95	0.361	1.71E-10	1.28E-10	39.2	8	102	1194	1.359	1.00	1.62	2270
AP	200	box	50	20	100	272	54	0.237	1.11E-10	5.65E-11	4.6	3	101	880	1.735	1.50	1.86	375
AP	200	tube	52	35	200	374	74	0.337	1.06E-10	1.07E-10	20.0	6	136	402	1.418	1.00	1.96	4659
AP	200	tube	52	35	200	374	74	0.398	7.97E-11	1.67E-10	21.8	6	144	530	1.345	1.00	1.71	2509
AP	100	box	100	35	100	953	190	0.248	1.27E-10	5.33E-11	7.3	3	271	464	1.338	1.00	1.76	325
AP	100	box	500	35	100	4765	953	0.200	1.09E-10	3.92E-11	41.0	6	178	513	1.490	1.00	1.97	743
AP	100	box	50	35	100	476	95	0.238	7.32E-11	4.87E-11	5.1	3	108	919	1.368	1.00	1.61	270
AP	100	box	50	20	100	272	54	0.179	8.94E-11	2.96E-11	2.6	6	102	505	1.489	1.00	1.91	1315
AP	100	box	100	35	100	953	190	0.249	1.89E-10	6.35E-11	46.0	5	301	1633	1.282	1.00	1.59	565
AP	100	box	100	35	100	953	190	0.251	1.13E-10	5.77E-11	14.2	5	283	740	1.546	1.00	1.95	731
AP	100	box	250	35	100	2382	476	0.348	4.12E-10	1.60E-10	84.5	1	184	184	1.454	1.45	1.45	398
AP	100	box	50	35	100	476	95	0.245	1.08E-10	5.56E-11	9.0	2	108	159	1.473	1.39	1.56	237
AP	20	box	50	35	100	476	47	0.276	6.06E-11	3.01E-10	125.8	4	2155	2580	0.765	0.72	0.86	4782
AP	20	box	50	35	100	476	95	0.157	5.81E-11	1.86E-11	1.6	2	141	1155	1.615	1.59	1.64	210
AP	20	box	50	35	100	476	95	0.178	5.81E-11	2.57E-11	3.8	5	130	838	1.338	1.00	1.59	215
AP	20	box	50	35	100	476	95	0.179	6.17E-11	2.61E-11	1.2	4	120	1176	1.454	1.00	1.64	204
AP	20	box	50	35	100	476	95	0.201	7.20E-11	5.14E-11	44.7	7	457	1860	1.336	1.00	1.91	1512
AP	20	box	50	35	100	476	95	0.207	7.91E-11	4.00E-11	15.2	4	107	4085	1.646	1.40	1.92	365
AP	20	box	50	20	100	272	54	0.134	8.78E-11	1.35E-11	1.8	0						
AP	20	box	100	35	100	953	190	0.216	8.99E-11	6.47E-11	155.9	5	109	4567	1.588	1.30	1.94	573
AP	20	box	250	35	100	2382	476	0.221	1.29E-10	6.15E-11	111.5	3	166	8197	1.580	1.51	1.70	345
AP	20	box	500	35	100	4765	953	0.133	5.92E-11	1.91E-11	107.3	3	229	10127	1.527	1.28	1.75	223
AP	20	box	50	35	100	476	95	0.177	8.17E-11	3.34E-11	39.1	5	387	1197	1.254	1.00	1.62	1312
AP	20	box	50	20	100	272	54	0.139	4.11E-11	1.69E-11	1.5	0						
AP	20	tube	52	35	200	374	74	0.182	6.11E-11	2.74E-11	4.5	4	102	544	1.358	1.00	1.73	1093
NAP	20	box	50	35	100	476	95	0.278	1.18E-10	8.74E-11	42.3	2	7090	7933	1.736	1.72	1.75	363
NAP	20	box	100	35	100	953	190	0.234	9.82E-11	6.22E-11	70.8	4	756	4044	1.472	1.23	1.77	558
NAP	20	box	250	35	100	2382	476	0.221	1.37E-10	6.36E-11	295.1	3	1731	8573	1.568	1.29	1.84	375
NAP	20	box	500	35	100	4765	953	0.165	1.09E-10	5.05E-11	862.8	1	3867	3867	1.177	1.18	1.18	464
NAP	20	box	50	35	100	476	95	0.176	5.70E-11	2.72E-11	4.7	4	110	1216	1.480	1.00	1.76	279
NAP	20	box	50	35	100	476	95	0.209	1.12E-10	4.67E-11	16.1	2	1030	2223	1.708	1.59	1.83	256
NAP	20	box	50	35	100	370	74	0.345	3.06E-10	1.46E-10	21.0	0						
NAP	20	box	50	35	400	476	95	0.398	1.72E-10	1.50E-10	28.8	8	454	1118	1.490	1.00	1.98	2180
NAP	20	box	50	35	400	476	95	0.460	1.61E-10	2.07E-10	15.2	3	115	2879	1.552	1.30	1.85	1342
NAP	20	box	50	35	400	370	74	0.559	2.73E-10	2.89E-10	10.5	2	1180	1567	1.753	1.66	1.85	839
NAP	20	box	50	35	100	476	95	0.267	7.93E-11	7.36E-11	28.3	8	102	3119	1.467	1.00	1.94	1759
NAP	20	box	50	35	100	476	95	0.231	1.02E-10	4.89E-11	21.9	4	498	2012	1.562	1.28	1.88	432
NAP	20	box	50	35	100	370	74	0.268	1.46E-10	7.13E-11	14.0	2	869	1901	1.719	1.68	1.76	393
NAP	20	box	50	35	400	476	95	0.439	1.62E-10	1.73E-10	9.7	0						
NAP	20	box	50	35	400	476	95	0.364	1.44E-10	1.09E-10	2.7	3	189	1145	1.333	1.00	1.52	536
NAP	20	box	50	35	400	370	74	0.536	2.06E-10	2.47E-10	10.3	2	776	1308	1.757	1.69	1.83	619
NAP	20	box	100	35	100	953	190	0.304	1.91E-10	9.95E-11	36.1	2	9172	9529	1.516	1.50	1.53	471
NAP	20	box	500	35	100	4765	953	0.225	1.44E-10	5.95E-11	65.6	2	110	9762	1.820	1.72	1.92	301
NAP	20	box	50	35	100	476	95	0.219	1.25E-10	4.84E-11	14.7	6	105	1707	1.597	1.37	1.88	513
NAP	20	tube	52	35	200	374	74	0.204	5.31E-11	3.09E-11	5.3	3	108	474	1.770	1.55	1.91	268
NAP	20	tube	52	35	200	374	74	0.225	4.39E-11	4.48E-11	7.1	7	123	298	1.423	1.00	1.91	4797
NAP	20	box	50	35	100	476	95	0.332	1.36E-10	1.11E-10	34.1	5	1044	2692	1.546	1.22	1.88	718
NAP	20	box	50	35	100	476	95	0.252	1.06E-10	5.32E-11	3.1	4	113	1053	1.438	1.00	1.73	296
NAP	20	box	50	35	100	476	95	0.214	6.32E-11	4.07E-11	12.9	4	147	738	1.313	1.00	1.47	360
NAP	20	box	50	35	100	476	95	0.199	7.55E-11	3.65E-11	20.0	5	107	1049	1.325	1.00	1.73	1386
NAP	20	box	50	35	100	476	95	0.328	1.26E-10	1.17E-10	38.2	2	11308	12913	1.879	1.84	1.92	421
NAP	20	box	50	35	100	476	95	0.278	1.18E-10	9.06E-11	42.3	2	7090	7933	1.736	1.72	1.75	378

References

1. P. Harrison, *Blood Reviews* **19**, 111–123, ISSN: 0268960X (2005).
2. N. J. Breet *et al.*, *JAMA - Journal of the American Medical Association* **303**, 754–762, ISSN: 00987484 (2010).
3. S. M. Picker, *Transfusion and Apheresis Science* **44**, 305–319, ISSN: 14730502 (2011).
4. K. Koltai, G. Kesmarky, G. Feher, A. Tibold, K. Toth, *International Journal of Molecular Sciences* **18**, 1803, ISSN: 1422-0067, (<http://www.mdpi.com/1422-0067/18/8/1803>) (2017).
5. J. W. Weisel, R. I. Litvinov, *Journal of Thrombosis and Haemostasis* **17**, 271–282 (2019).
6. M. H. Flamm, S. L. Diamond, *Annals of Biomedical Engineering* **40**, 2355–2364, ISSN: 15739686 (2012).
7. A. L. Zydney, C. K. Colton, *PCH. Physicochemical hydrodynamics* **10**, 77–96, ISSN: 01919059 (1988).
8. K. Affeld, L. Goubergrits, N. Watanabe, U. Kertzscher, *Journal of Biomechanics* **46**, 430–436, ISSN: 00219290 (2013).
9. B. Chopard *et al.*, *Royal Society Open Science* **4**, 170219, ISSN: 2054-5703, (<https://royalsocietypublishing.org/doi/10.1098/rsos.170219>) (2017).
10. L. Crowl, A. L. Fogelson, *Journal of Fluid Mechanics* **676**, 348–375, ISSN: 14697645 (2011).
11. H. Zhao, E. S. Shaqfeh, *Physical Review E - Statistical, Nonlinear, and Soft Matter Physics* **83**, 061924, ISSN: 15393755 (2011).
12. H. Zhao, E. S. Shaqfeh, V. Narsimhan, *Physics of Fluids* **24**, 011902, ISSN: 10706631, (<http://aip.scitation.org/doi/10.1063/1.3677935>) (2012).
13. D. A. Reasor, M. Mehrabadi, D. N. Ku, C. K. Aidun, *Annals of Biomedical Engineering* **41**, 238–249, ISSN: 00906964 (2013).
14. K. Vahidkhah, S. L. Diamond, P. Bagchi, *Biophysical Journal* **106**, 2529–2540, ISSN: 15420086 (2014).
15. M. Mehrabadi, D. N. Ku, C. K. Aidun, *Annals of Biomedical Engineering* **43**, 1410–1421, ISSN: 15739686 (2015).
16. M. Mehrabadi, D. N. Ku, C. K. Aidun, *Physical Review E* **93**, 023109, ISSN: 24700053 (2016).
17. E. C. Eckstein, F. Belgacem, *Biophysical Journal* **60**, 53–69, ISSN: 00063495 (1991).
18. A. Kumar, M. D. Graham, *Soft Matter* **8**, 10536–10548, ISSN: 17446848 (2012).
19. K. Vahidkhah, P. Bagchi, *Soft Matter* **11**, 2097–2109, ISSN: 17446848 (2015).
20. T. R. Lee *et al.*, *Scientific Reports* **3**, 1–8, ISSN: 20452322 (2013).
21. K. Yeo, M. R. Maxey, *EPL (Europhysics Letters)* **92**, 24008, ISSN: 0295-5075 (2010).
22. M. Gross, T. Krüger, F. Varnik, *EPL (Europhysics Letters)* **108**, 68006, ISSN: 0295-5075 (2014).
23. C. Kleiber, S. Kotz, *Statistical Size Distributions in Economics and Actuarial Sciences* (John Wiley & Sons, Inc., Hoboken, NJ, USA, 2003), ISBN: 0471150649, (<http://doi.wiley.com/10.1002/0471457175>).
24. C. Kotsalos, J. Latt, B. Chopard, *Journal of Computational Physics* **398**, 108905, ISSN: 10902716 (2019).
25. C. Kotsalos, J. Latt, J. Beny, B. Chopard, *Interface Focus (accepted for publication)*, arXiv: 1911.03062 (2020).
26. J. Latt *et al.*, *Computers and Mathematics with Applications*, ISSN: 08981221 (2020).
27. K. Z. Boudjeltia *et al.*, *medRxiv* (2020).
28. A. Clauset, C. R. Shalizi, M. E. Newman, *Power-law distributions in empirical data*, 2009.
29. N. N. Taleb, *Statistical Consequences of Fat Tails: Real World Preasymptotics, Epistemology, and Applications (Technical Incerto)* (STEM Academic Press, ed. 1, 2020), vol. 1, p. 446, ISBN: 1544508050, arXiv: 2001.10488, (<https://arxiv.org/abs/2001.10488>).
30. J. Alstott, E. Bullmore, D. Plenz, *PLoS ONE* **9**, e85777, ISSN: 19326203 (2014).
31. W. Jy, L. L. Horstman, D. Homolak, Y. S. Ahn, *Platelets* **6**, 354–358, ISSN: 09537104 (1995).
32. J. J. Betts, J. P. Betts, J. T. Nicholson, *Significance of ADP, plasma and platelet concentration in platelet electrophoretic studies*, 1968.
33. J. R. Hampton, J. R. Mitchell, *Nature* **210**, 1000–1002, ISSN: 00280836 (1966).
34. R. Dutta *et al.*, *Frontiers in Physiology* **9**, 1128, ISSN: 1664-042X, (<https://www.frontiersin.org/article/10.3389/fphys.2018.01128/full>) (2018).

Acknowledgments

We acknowledge support from the Swiss National Supercomputing Center (CSCS, Piz-Daint supercomputer), the National Supercomputing Center in the Netherlands (Surfsara, Cartesius supercomputer), and the HPC Facilities of the University of Geneva (Baobab cluster).

Source Code

The source code for the statistical analysis is available in GitHub: <https://github.com/kotsaloscvcv/PLTs-FatTails>. The tools for performing the cellular blood flow simulations, as presented in Kotsalos et al. (24, 25), are available as part of Palabos open-source library (npFEM specialized module): <https://palabos.unige.ch>.

Funding

This project has received funding from the European Union’s Horizon 2020 research and innovation programme under grant agreement No 823712 (CompBioMed2 project). Furthermore, this work was supported by grants from the CHU Charleroi; the Fonds pour la Chirurgie Cardiaque; Fonds de la Recherche Medicale en Hainaut (FRMH) and by the Swiss PASC project “Virtual Physiological Blood: an HPC framework for blood flow simulations in vasculature and in medical devices”.

Authors’ contributions

C.K and B.C. wrote the paper. C.K. performed the research, carried out the simulations and the analysis of the results. K.Z.B. supervised the research and revised the manuscript. R.D. supervised the research and revised the manuscript. J.L. wrote part of the computational framework, supervised the research and revised the manuscript. B.C. conceived and supervised the research and revised the manuscript. All authors approved the final version of the manuscript.

Competing interests

The authors declare that they have no competing interests.